

# Dark energy and neutrino constraints from a future EUCLID-like survey

Tobias Basse<sup>a</sup> Ole Eggers Bjælde<sup>a</sup> Jan Hamann<sup>b</sup> Steen Hannestad<sup>a</sup>  
Yvonne Y.Y. Wong<sup>c,1</sup>

<sup>a</sup>Department of Physics and Astronomy  
University of Aarhus, DK-8000 Aarhus C, Denmark

<sup>b</sup>Theory Division, Physics Department  
CERN, CH-1211 Geneva 23, Switzerland

<sup>c</sup>Institut für Theoretische Teilchenphysik und Kosmologie  
RWTH Aachen, D-52056 Aachen, Germany

E-mail: [basse@phys.au.dk](mailto:basse@phys.au.dk), [oeb@phys.au.dk](mailto:oeb@phys.au.dk), [jan.hamann@cern.ch](mailto:jan.hamann@cern.ch),  
[sth@phys.au.dk](mailto:sth@phys.au.dk), [yvonne.wong@physik.rwth-aachen.de](mailto:yvonne.wong@physik.rwth-aachen.de)

**Abstract.** We perform a detailed forecast on how well a EUCLID-like survey will be able to constrain dark energy and neutrino parameters from a combination of its cosmic shear power spectrum, galaxy power spectrum, and cluster mass function measurements. We find that the combination of these three probes vastly improves the survey’s potential to measure the time evolution of dark energy. In terms of a dark energy figure-of-merit defined as  $(\sigma(w_0)\sigma(w_a))^{-1}$ , we find a value of 454 for EUCLID-like data combined with PLANCK-like measurements of the cosmic microwave background (CMB) anisotropies in a fiducial  $\Lambda$ CDM cosmology, a number that is quite conservative compared with existing estimates because of our choice of model parameter space and analysis method, but still represents a factor of 3 to 8 improvement over using either CMB+galaxy clustering+cosmic shear data, or CMB+cluster mass function alone. We consider also the survey’s potential to measure dark energy perturbations in models wherein the dark energy is parameterised as a fluid with a nonstandard non-adiabatic sound speed, and find that in an *optimistic* scenario in which  $w_0$  deviates by as much as is currently observationally allowed from  $-1$ , models with  $\hat{c}_s^2 = 10^{-6}$  and  $\hat{c}_s^2 = 1$  can be distinguished at more than  $2\sigma$  significance. Under the same optimistic assumptions, if the Jeans mass associated with dark energy clustering falls within the cluster mass range observed by the survey, then the order of magnitude of the dark energy sound speed can potentially be pinned down. Finally, we find that the sum of neutrino masses can be measured with a  $1\sigma$  precision of 0.01 eV, even in complex cosmological models in which the dark energy equation of state varies with time. The  $1\sigma$  sensitivity to the effective number of relativistic species  $N_{\text{eff}}^{\text{ml}}$  is approximately 0.02, meaning that the small deviation of 0.046 from 3 in the standard value of  $N_{\text{eff}}^{\text{ml}}$  due to non-instantaneous decoupling and finite temperature effects can be probed with  $2\sigma$  precision for the first time.

---

<sup>1</sup>Present address: School of Physics, The University of New South Wales, Sydney NSW 2052, Australia

---

## Contents

<b>1</b>	<b>Introduction</b>	<b>1</b>
<b>2</b>	<b>Dark energy parameterisation</b>	<b>2</b>
<b>3</b>	<b>The cluster mass function as a EUCLID observable</b>	<b>3</b>
3.1	Cluster mass function from theory	3
3.2	The observable	5
<b>4</b>	<b>Measurement errors</b>	<b>5</b>
4.1	Redshift uncertainty	5
4.2	Uncertainty in the weak lensing mass determination	5
<b>5</b>	<b>Mock data generation</b>	<b>6</b>
5.1	Mass detection threshold	6
5.2	Redshift and mass binning	8
5.3	Completeness and efficiency	8
5.4	Synthetic data sets	9
<b>6</b>	<b>Forecasting</b>	<b>9</b>
6.1	Model parameter space	9
6.2	Likelihood function	10
<b>7</b>	<b>Results</b>	<b>10</b>
7.1	Impact of the number of bins	10
7.2	Probes of the expansion history versus probes of the power spectrum	12
7.3	Combining all data sets: constraints on neutrino parameters	13
7.4	The dark energy figure-of-merit	14
7.5	Dark energy sound speed and perturbations	15
<b>8</b>	<b>Conclusions</b>	<b>17</b>
<b>A</b>	<b>Interpolating the spherical collapse between the two limits of <math>\hat{c}_s^2</math></b>	<b>18</b>

---

## 1 Introduction

The coming decade will see spectacular advances in the measurement of the large-scale structure distribution in the universe. Perhaps the most interesting of these measurements are the large-scale photometric surveys to be conducted by the Large Synoptic Survey Telescope (LSST) [1] and the ESA EUCLID mission [2]. Both projects will map the positions and measure the shapes of order a billion galaxies in a significant fraction of the current Hubble volume. This will in turn allow for a precision measurement of both the galaxy clustering and the cosmic shear power spectra, and likewise an impressively precise determination of the cosmological parameter values. As an example, assuming a vanilla  $\Lambda$ CDM model extended with nonzero neutrino masses, a EUCLID-like survey will be able to measure the neutrino mass sum  $\sum m_\nu$  most optimistically at the 0.01 eV level of precision [3] when

combined with measurements of the cosmic microwave background (CMB) anisotropies from the Planck mission [4]. Such a precision will see the absolute neutrino mass scale detected at  $5\sigma+$  confidence even if the true value of  $\sum m_\nu$  should be the minimum compatible with current neutrino oscillation data, i.e.,  $\sum m_\nu \simeq 0.06$  eV [3].

As yet unexplored in reference [3] is the role played by the cluster mass function in cosmological parameter inference. Weak gravitational lensing measurements available to both the LSST and EUCLID will allow for the efficient detection and mass determination of galaxy clusters; EUCLID, for example, is expected to detect and accurately measure the masses of close to 100 000 clusters [2]. In this work, we continue the cosmological parameter sensitivity forecast begun in [3] by adding the cluster mass function inferred from a EUCLID-like cluster survey to the galaxy and the shear power spectra measurements already considered in reference [3]. We also extend the study to dark energy models with a time-dependent equation of state and/or a nonstandard non-adiabatic sound speed. As in [3] we shall adopt the survey specifications of the EUCLID mission in terms of the number of objects observed, the redshift range, and the sky coverage. However, the analysis procedure can be easily adapted to other similar redshift surveys such as the LSST.

The paper is structured as follows. We discuss first our dark energy parametrisation in section 2, before introducing in section 3 the cluster mass function as a cosmological observable. In section 4 we examine some uncertainties likely to be encountered in a EUCLID-like measurement of the cluster mass function, and discuss how we model and propagate these uncertainties in our forecast analysis. Sections 5 and 6 outline respectively our mock data generation and forecast procedures, while section 7 contains our results. We conclude in section 8.

## 2 Dark energy parameterisation

Although dark energy is the most popular explanation for the apparent accelerated expansion of the universe, there is as yet no consensus on its actual physical properties. For this reason, and for reasons of simplicity, dark energy is usually described as a fluid obeying the laws of general relativity. The homogeneous part of this fluid is responsible for driving the expansion of the universe, and can be represented by an equation of state  $w(\tau) = \bar{P}_Q(\tau)/\bar{\rho}_Q(\tau)$ , where  $\bar{P}_Q(\tau)$  and  $\bar{\rho}_Q(\tau)$  denote the unperturbed dark energy pressure and energy density respectively, and  $\tau$  is conformal time. Except in the case of a cosmological constant, for which  $w(\tau)$  is precisely the constant  $-1$ , dynamical dark energy models have in general equations of state that are functions of time. For this reason, we model dark energy equation of state using the popular parametrisation [5, 6]

$$w(\tau) = w_0 + w_a[1 - a(\tau)], \quad (2.1)$$

where  $w_0$  and  $w_a$  are constants, and  $a(\tau)$  denotes the scale factor. Note that this parameterisation should be regarded simply as a toy model that facilitates comparisons across different observational probes. We make no pretence here that it actually captures the behaviour of any realistic dynamic dark energy model. For an example of a forecast tailored specifically to scalar-field models of dark energy, see, e.g., [7].

A general relativistic fluid evolving in an inhomogeneous spacetime will in general develop inhomogeneities of its own. We express inhomogeneities in the dark energy density in terms of a density contrast  $\delta_Q(\tau, \mathbf{x})$  satisfying  $\rho_Q(\tau, \mathbf{x}) = \bar{\rho}_Q(\tau)[1 + \delta_Q(\tau, \mathbf{x})]$ , where  $\rho_Q(\tau, \mathbf{x})$  is the fully time- and space-dependent dark energy density.

Evolution of the density contrast  $\delta_Q(\tau, \mathbf{x})$  can be described by a set of (nonlinear) fluid equations coupled to the (nonlinear) Einstein equation. For the nonlinear aspects of the formation of clusters we refer to section 3.1 and appendix A. For the purpose of calculating the linear matter power spectrum we implement the linear evolution for the dark energy density contrast, described in the synchronous gauge and in Fourier space by the equations of motion (see, e.g., [8, 10–12])

$$\begin{aligned} \dot{\delta}_Q + (1+w) \left( \theta_Q + \frac{\dot{h}}{2} \right) + 3(\hat{c}_s^2 - w)\mathcal{H}\delta_Q + 9(1+w)(\hat{c}_s^2 - c_a^2)\mathcal{H}^2 \frac{\theta_Q}{k^2} &= 0, \\ \dot{\theta}_Q + (1-3\hat{c}_s^2)\mathcal{H}\theta_Q - \frac{\hat{c}_s^2 k^2}{1+w} \delta_Q + k^2 \sigma_Q &= 0, \end{aligned} \quad (2.2)$$

where  $\delta_Q(\tau, k)$  now denotes the dark energy density contrast in Fourier  $k$ -space,  $\theta_Q(\tau, k)$  is the divergence of the dark energy velocity field,  $h$  the metric perturbation,  $\mathcal{H} \equiv \dot{a}/a$  the conformal Hubble parameter, and  $\hat{c}_s^2 \equiv \delta P_Q / \delta \rho_Q|_{\text{rest}}$  and  $c_a^2 \equiv \dot{P}_Q / \dot{\rho}_Q$  are the non-adiabatic and adiabatic dark energy sound speeds respectively. Note that the non-adiabatic sound speed  $\hat{c}_s^2$  is defined as the ratio of the pressure perturbation  $\delta P_Q$  to the energy density perturbation  $\delta \rho_Q$  in the rest-frame of the dark energy fluid, while the adiabatic sound speed  $c_a^2$  is related to the homogeneous fluid equation of state via  $\dot{w} = 3(1+w)(w - c_a^2)\mathcal{H}$ .

### 3 The cluster mass function as a EUCLID observable

Cluster surveys can be an excellent probe of dynamical dark energy because the abundance of the most massive gravitationally bound objects at any one time depends strongly on both the growth function of the matter perturbations and the late-time expansion history of the universe (see, e.g., [13–18]). The EUCLID mission will identify clusters in the photometric redshift survey accompanied by a spectroscopic follow-up. The same survey will also determine the masses of the detected clusters by way of weak gravitational lensing (cosmic shear).

#### 3.1 Cluster mass function from theory

A simple quantification of the cluster distribution is the cluster mass function. Denoted  $dn/dM(M, z)$ , the cluster mass function counts the number of clusters per comoving volume in a given mass interval  $[M, M + dM]$  as a function of redshift  $z$ .

For any given cosmological model, an accurate prediction of the corresponding cluster mass function necessitates the use of  $N$ -body/hydrodynamics simulations. However, a number of fitting functions, calibrated against simulation results in the vanilla  $\Lambda$ CDM model framework, have been proposed in the literature (e.g., [19–21]). In this work, we model the cluster mass function after the Sheth-Tormen fitting function [19]

$$\frac{dn_{\text{ST}}}{dM}(M, z) = -\sqrt{\frac{2a}{\pi}} A \left[ 1 + \left( \frac{a\delta_c^2}{\sigma_m^2} \right)^{-p} \right] \frac{\bar{\rho}_m}{M^2} \frac{\delta_c}{\sigma_m} \frac{d \log \sigma_m}{d \log M} \exp \left[ -a \frac{\delta_c^2}{2\sigma_m^2} \right], \quad (3.1)$$

where the fitting parameters are  $a = 0.707$ ,  $A = 0.322184$ , and  $p = 0.3$ , and  $\bar{\rho}_m(z)$  is the mean matter density (it was shown in [45] that this yields a very good fit also in models with non-zero neutrino mass). The quantity  $\sigma_m^2(M, z)$  denotes the variance of the linear matter density field smoothed on a comoving length scale  $X_{\text{sm}} \equiv a^{-1}[3M/(4\pi\bar{\rho}_m)]^{1/3}$ , and is

computed from the linear matter power spectrum  $P_m^{\text{lin}}(k, z)$  via

$$\sigma_m^2(M, z) \equiv \frac{1}{2\pi^2} \int_0^\infty dk k^2 |W(kX_{\text{sm}})|^2 P_m^{\text{lin}}(k, z), \quad (3.2)$$

where  $W(x) = 3(\sin x - x \cos x)/x^3$  is the Fourier transform of the spherical (spatial) top-hat filter function. The linear power spectrum  $P_m^{\text{lin}}(k, z)$  can be obtained from a Boltzmann code such as CAMB [22].

The quantity  $\delta_c(M, z)$  is known as the linear threshold density of matter at the time of collapse. Its value is established by tracking the full nonlinear collapse of a spherical top-hat over-density, noting the time  $\tau_{\text{coll}}$  the region collapses to an infinitely dense point, and then computing from *linear* perturbation theory the *linear* density contrast at  $\tau = \tau_{\text{coll}}$ . In many applications it suffices to take the constant value  $\delta_c = 1.68$ . In dark energy cosmologies, however, this may not be a very good approximation (see, e.g., [9, 23]). Here, we estimate  $\delta_c(M, z)$  as described immediately above, and track the spherical collapse of a top-hat overdensity by solving the equations

$$\frac{\ddot{X}}{X} + \mathcal{H} \frac{\dot{X}}{X} = -\frac{4\pi G}{3} a^2 [\bar{\rho}_m \delta_m + \bar{\rho}_Q (1 + 3\hat{c}_s^2) \delta_Q], \quad (3.3)$$

$$\delta_m(\tau) = [1 + \delta_m(\tau_i)] \left[ \frac{X(\tau_i)}{X(\tau)} \right]^3 - 1, \quad (3.4)$$

where  $X(\tau)$  is the comoving radius of the top-hat,  $\delta_m(\tau)$  and  $\delta_Q(\tau)$  the matter and dark energy density contrasts respectively in the top-hat region, and  $\tau_i$  is a reference initial time. Note that equation (3.4) follows from conservation of the total mass of nonrelativistic matter  $M_m$  in the top-hat region. For more detailed discussions of the spherical collapse model, we direct the reader to references [24–26].

The presence of the  $\bar{\rho}_Q(1 + 3\hat{c}_s^2)\delta_Q$  term on the right hand side of equation (3.3) indicates that the dark energy component also participates in the collapse, especially when the initial dimension  $X(\tau_i)$  of the top-hat matter overdensity exceeds the comoving Jeans length associated with the fluid’s non-adiabatic sound speed [9, 27–29]. The resulting linear threshold density  $\delta_c$  therefore exhibits generically a dependence on the mass of the collapsing region, in addition to the usual  $z$ -dependence. However, tracking the nonlinear evolution of the dark energy density contrast  $\delta_Q$  is in general nontrivial because the spherical top-hat region is well-defined strictly only in the  $\hat{c}_s^2 = 0$  and the  $\hat{c}_s^2 \rightarrow \infty$  limits, where, supplemented with [9, 28]

$$\bar{\rho}_Q(1 + 3\hat{c}_s^2)\delta_Q \rightarrow 0, \quad \hat{c}_s^2 \rightarrow \infty, \quad (3.5)$$

$$\dot{\rho}_Q + 3 \left( \mathcal{H} + \frac{\dot{X}}{X} \right) (\rho_Q + \bar{P}_Q) = 0, \quad \hat{c}_s^2 = 0, \quad (3.6)$$

the collapse equation (3.3) can be solved exactly. Extending the application of equation (3.3) to the intermediate regime necessitates additional assumptions, which do not however render the system any less intractable [9, 29]. For this reason, we shall resort to modelling the mass-dependence of  $\delta_c(M, z)$  by interpolating between the two known limits using a hyperbolic tangent function, where the location of the kink at each redshift is adjusted to reflect the Jeans mass corresponding to the given  $\hat{c}_s^2$ . See appendix A for details.

Finally, the virial radius  $R_{\text{vir}}$  and the virial mass  $M_{\text{vir}}$  can likewise be computed from equations (3.3) to (3.6) in the two limits of  $\hat{c}_s^2$ . Here,  $R_{\text{vir}} \equiv aX(\tau_{\text{vir}})$  is defined as the physical

radius of the top-hat region and  $M_{\text{vir}}$  the total mass contained therein at virialisation, where virialisation is taken to mean the moment at which the virial theorem is satisfied by the collapsing region,  $\tau_{\text{vir}}$ . The virial mass  $M_{\text{vir}} = M_{\text{m}} + M_Q(\tau_{\text{vir}})$  counts both contributions from nonrelativistic matter  $M_{\text{m}}$  and from the clustered dark energy  $M_Q \equiv (4\pi/3)\bar{\rho}_Q\delta_Q(aX)^3$ , and it is  $M_{\text{vir}}$ , not  $M_{\text{m}}$ , that we identify with the cluster mass  $M$  throughout this work. Further details can be found in appendix A. The virial radius will be used in section 5.1 to determine the cluster mass detection threshold.

### 3.2 The observable

The actual observable quantity is the number of clusters  $N_{i,j(i)}$  in the redshift bin  $i$  and the (redshift-dependent) mass bin  $j(i)$ , defined as

$$N_{i,j(i)} = \Delta\Omega \int_0^\infty dz \int_0^\infty dM \frac{d^2V}{d\Omega dz}(z) W_{i,j(i)}(M, z) \frac{dn}{dM}(M, z), \quad (3.7)$$

where  $\Delta\Omega$  is the solid angle covered by the survey,  $d^2V/(d\Omega dz)(z)$  the comoving volume element at redshift  $z$ , and  $W_{i,j(i)}(M, z)$  is the window function defining the redshift and mass bin. Note that the window functions are in general not sharp in  $z$ - and  $M$ -space because of uncertainties in the redshift and the mass determinations (see sections 4.1 and 4.2). We defer the discussion of our binning scheme to section 5.2.

## 4 Measurement errors

### 4.1 Redshift uncertainty

The EUCLID photometric survey will measure redshifts with an estimated scatter of  $\sigma(z) \sim 0.03(1+z)$  and almost no bias [2]. Nonetheless, because the detected clusters will be subject to a follow-up spectroscopic study, the effective uncertainty in the redshift determination *per se* can be taken as negligible. Additional redshift errors may arise from the peculiar velocities of the clusters, where velocities up to  $\sim 1000 \text{ km s}^{-1}$  may lead to an error of  $\delta z \sim 0.003$ . However, as we shall see in section 5.2, even the narrowest redshift bins adopted in our analysis typically have widths of order  $\Delta z \sim 0.03$ , i.e., a factor of ten larger than the peculiar velocity uncertainty. We therefore treat the cluster redshift as infinitely well-determined, and approximate the window function of the redshift bin  $i$  as

$$V_i(z) = \theta(z - z_{\text{min},i})\theta(z_{\text{max},i} - z), \quad (4.1)$$

where  $z_{\text{min},i}$  and  $z_{\text{max},i}$  denote, respectively, the lower and upper boundaries of the bin.

### 4.2 Uncertainty in the weak lensing mass determination

The mass of a cluster determined through weak lensing,  $M_{\text{obs}}$ , is subject to scatter and bias with respect to the true mass of the cluster  $M$  [30, 31]. For a mass determination algorithm that treats clusters as spherical objects, the triaxiality of realistic cluster density profiles, for example, could cause the cluster mass to be over- or underestimated depending on the orientation of the major axis in relation to the line-of-sight. Additional biases are incurred if the true density profile deviates from the assumed one.

In this work, we assume that the bias can be controlled to the required level of accuracy, and model only the scatter in the mass determination using a log-normal distribution [30, 31],

$$P(M_{\text{obs}}|M) = \frac{1}{M_{\text{obs}}\sqrt{2\pi\sigma^2}} \exp\left[-\frac{(\ln M_{\text{obs}} - \mu)^2}{2\sigma^2}\right]. \quad (4.2)$$

Here,  $P(M_{\text{obs}}|M)$  denotes the probability that a cluster with true mass  $M$  is determined to have a mass  $M_{\text{obs}}$  by the survey, and  $\mu$  and  $\sigma$  are, respectively, the median and the standard deviation of the distribution. Since we assume an unbiased mass determination, the mean of the distribution is  $M$  and thus  $\mu = \ln M - \sigma^2/2$ . We use  $\sigma = 0.2$  to model the mass scatter.

The distribution (4.2) can be integrated over  $M_{\text{obs}}$  in the interval  $[M_{\text{min},j(i)}, M_{\text{max},j(i)}]$  in order to determine the probability that a cluster of true mass  $M$  in the redshift bin  $i$  will be determined to lie in the mass bin  $j(i)$ . Combing the resulting integral with the redshift window function  $V_i(z)$  from equation (4.1), we obtain the window function for the redshift and mass bin  $\{i, j(i)\}$ ,

$$W_{i,j(i)}(M, z) = \theta(z - z_{\text{min},i})\theta(z_{\text{max},i} - z) \int_{M_{\text{min},j(i)}}^{M_{\text{max},j(i)}} dM_{\text{obs}} P(M_{\text{obs}}|M) \theta(M_{\text{obs}} - M_{\text{thr}}(z)), \quad (4.3)$$

where  $M_{\text{thr}}(z)$  is the mass detection threshold, to be discussed in section 5.1.

## 5 Mock data generation

The observable quantity in a cluster survey is the number of clusters  $N_{i,j(i)}$  in the redshift bin  $i$  and mass bin  $j(i)$ . Thus for any given fiducial cosmology and survey specifications, one may compute the fiducial cluster numbers  $N_{i,j(i)}^{\text{fid}}$  as per equation (3.7), and then create a mock data set  $\hat{N}_{i,j(i)}$  by assuming  $\hat{N}_{i,j(i)}$  to be a stochastic variable that follows a Poisson distribution with parameter  $N_{i,j(i)}^{\text{fid}}$ . An ensemble of realisations may be generated by repeating the procedure multiple times, and parameter inference performed on each mock realisation in order to assess the performance of a survey.

This is clearly a very lengthy process. However, as shown in reference [32], for the sole purpose of establishing a survey's sensitivity to cosmological parameters, it suffices to use only one mock data set in which the data points are set to be equal to the predictions of the fiducial model, i.e.,  $\hat{N}_{i,j(i)} = N_{i,j(i)}^{\text{fid}}$ . This much simplified procedure correctly reproduces the survey sensitivities in the limit of infinitely many random realisations, and is the procedure we adopt in our analysis.

In the following we describe in some detail the survey specifications that go into the computation of the fiducial  $N_{i,j(i)}^{\text{fid}}$ : the mass detection threshold, our redshift and mass binning scheme, and the survey completeness and efficiency. In section 5.4 we summarise the mock data sets to be used in our parameter sensitivity forecast.

### 5.1 Mass detection threshold

We model the redshift-dependent mass detection threshold  $M_{\text{thr}}(z)$  following the approach of references [13, 33]. A cluster of mass  $M$  at redshift  $z$  produces a shear signal  $\kappa_G(M, z)$ , where

$$\kappa_G(M, z) = \alpha(M, z) \frac{M/[\pi R_s^2(M, z)]}{\Sigma_{\text{cr}}(z)}. \quad (5.1)$$



Here, assuming a truncated Navarro-Frenk-White (NFW) density profile [34],  $R_s(M, z) = R_{\text{vir}}(M, z)/c_{\text{nfw}}$ , where  $R_{\text{vir}}$  is the cluster's virial radius computed according to the spherical collapse model outlined in section 3.1 and appendix A, and  $c_{\text{nfw}} = 5$  is the halo concentration parameter determined from  $N$ -body simulations. The factor  $\alpha(M, z)$  is computed from smoothing the (projected) NFW profile using a Gaussian filter of angular smoothing scale  $\theta_G$ , i.e.,

$$\alpha(M, z) = \frac{\int_0^\infty dx (x/x_G^2) \exp(-x^2/x_G^2) f(x)}{\ln(1 + c_{\text{nfw}}) - c_{\text{nfw}}/(1 + c_{\text{nfw}})}, \quad (5.2)$$

where  $x \equiv \theta/\theta_s$  and  $x_G \equiv \theta_G/\theta_s$ , with  $\theta_s(M, z) = R_s(M, z)/d_A(z)$  and  $d_A(z)$  the angular diameter distance to the cluster. The projected NFW profile is encoded in the dimensionless surface density profile  $f(x)$ , which can be found in equation (7) of reference [33]. In our analysis we use an angular smoothing scale of  $\theta_G = 1$  arcmin.

The mean critical surface mass density  $\Sigma_{\text{cr}}(z)$  is, assuming a flat spatial geometry, given by the expression

$$\Sigma_{\text{cr}}^{-1}(z) = \frac{4\pi G}{(1+z)} n_{\text{bg}}^{-1} \int_z^\infty dz' \, dn/dz' \chi(z) [1 - \chi(z)/\chi(z')], \quad (5.3)$$

where  $\chi(z')$  denotes the comoving radial distance to the redshift  $z'$ , and  $(dn/dz')dz'$  is the number density of source galaxies per steradian at redshift  $(z', z' + dz')$ , normalised such that  $n_{\text{bg}} = \int_0^\infty dz' \, dn/dz'$  gives the source galaxy surface density. As in [3], we assume a galaxy redshift distribution of the form

$$\frac{dn}{dz} \propto \left(\frac{z}{z_0}\right)^2 \exp\left[-\left(\frac{z}{z_0}\right)^\beta\right], \quad (5.4)$$

where for a EUCLID-like survey we choose  $\beta = 1$ ,  $z_0 = 0.3$ , and a source galaxy surface density of  $n_{\text{bg}} = 40 \text{ arcmin}^{-2}$  [2].

In order for a cluster to be considered detected, its shear signal  $\kappa_G$  must exceed the “noise” of the survey  $\sigma_{\text{noise}}$  by a predetermined amount. Shear detection is limited firstly by the intrinsic ellipticity of the background galaxies, and secondly by the number of galaxy images lensed by the cluster that fall within the smoothing aperture. Thus, the noise term may be estimated as [35]

$$\sigma_{\text{noise}}^2 = \frac{\sigma_\epsilon^2}{4\pi\theta_G^2 n_{\text{bg}}}, \quad (5.5)$$

where  $\sigma_\epsilon$  denotes the mean dispersion of the galaxy intrinsic ellipticity, and we use  $\sigma_\epsilon = 0.1$  in our analysis [2].

Defining a signal-to-noise ratio of  $S/N = 4.5$  to be our detection threshold (consistent with a survey efficiency of  $e = 0.75$  [36], to be discussed in section 5.3), the expression

$$S/N = \frac{\kappa_G(M_{\text{thr}}(z), z)}{\sigma_{\text{noise}}} \quad (5.6)$$

can now be solved for the mass detection threshold  $M_{\text{thr}}(z)$ . This sets a lower limit on the cluster mass detectable by lensing at a given redshift  $z$ .



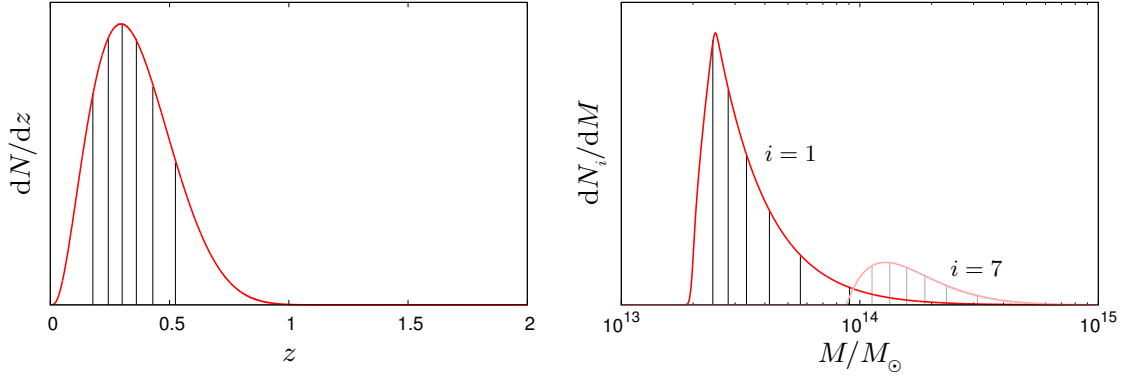


**Figure 1.** The left panel shows the division into of the observed number of clusters into 7 redshift bins while keeping the cluster count common for all bins. The right panel shows the subsequent division of redshift bins  $i = 1, 7$  into 7 mass bins, again with the stipulation that all mass bins contain the same number of clusters.

## 5.2 Redshift and mass binning

We consider a survey that observes clusters in the redshift range  $[z_{\text{low}}, z_{\text{high}}]$ . We subdivide this range into  $N_z$  bins in such a way so as to maintain the same number of clusters in all bins  $i$  in the fiducial cosmology. The resulting bin boundaries  $z_{\text{min},i}$  and  $z_{\text{max},i}$  then define the redshift window functions (4.1). Clusters in each redshift bin are further subdivided according to their observed masses into  $N_m$  mass bins labelled by  $j(i)$ , again with the enforcement that the number of clusters  $N_{i,j(i)}$  should be similar in all bins.

An immediate consequence of such a binning scheme is a variation of the mass bin boundaries  $M_{\text{min},j(i)}$  and  $M_{\text{max},j(i)}$  with redshift because of (i) the  $z$ -dependence of the mass detection threshold  $M_{\text{thr}}(z)$ , and (ii) the rarity of high-mass clusters at high redshifts. For the latter point, we impose in practice an absolute high-mass cut-off of  $M_{\text{high}} = 10^{16} M_\odot$ , i.e., the upper limit of the last mass bin,  $M_{\text{max},N_m(i)}$ , is always equal to  $M_{\text{high}}$  at all redshifts. This number also sets the high-redshift cut-off  $z_{\text{high}}$ , which is defined to be the redshift at which the mass detection threshold  $M_{\text{thr}}(z)$  exceeds  $M_{\text{high}}$ . The lower cut-off is set at  $z_{\text{low}} = 0.01$ , since the survey contains a negligible number of clusters below this redshift because of the small volume and a large detection threshold.

Figure 1 illustrates the division of the observed number of clusters into redshift and mass bins in the case  $N_z = N_m = 7$ . The left panel shows the first division in redshift, while the right panel shows the subsequent division of redshift bins  $i = 1, 7$  into mass bins.

## 5.3 Completeness and efficiency

The completeness of a cluster survey is defined as the fraction of clusters actually detected as peaks by the cluster finding algorithm, while the efficiency is the fraction of detected peaks that correspond to real clusters. In general these quantities can be established precisely only with the help of mock cluster catalogues generated from  $N$ -body simulations (see, e.g., [17, 33, 36–39]). Here, we adopt the same simplistic approach taken in reference [16], and assume both  $c$  and  $e$  to be mass- and redshift-independent. Then the effect of a survey completeness and efficiency not equal to unity amounts to increasing the uncertainty on each individual data point by a factor  $\sqrt{[(1/e - 1) + 1/e]/c}$ , which can be incorporated into the forecast analysis at the level of the likelihood function. We shall return to this point in section 6.2

where we discuss explicitly the construction of the likelihood function. Suffice it to say for now that we adopt the values  $c = 0.70$  and  $e = 0.75$ , which may be reasonably expected for the LSST [16], and which are likely very conservative when applied to EUCLID because of its much narrower point spread function.

#### 5.4 Synthetic data sets

We summarise here the mock EUCLID-like data sets we generate and use in our parameter sensitivity forecast.

- A cluster data set in the redshift range  $z \in [0.01, z_{\text{high}}]$ , and the mass range  $M \in [M_{\text{thr}}(z), 10^{16} M_{\odot}]$ , where  $M_{\text{thr}}(z)$  denotes the redshift-dependent mass detection threshold as described in section 5.1, and  $z_{\text{high}}$  is defined as the redshift at which  $M_{\text{thr}}(z)$  exceeds  $10^{16} M_{\odot}$  as discussed in section 5.2. We slice the redshift- and the mass-space into  $N_z$  and  $N_m$  bins respectively according to the scheme detailed in section 5.2.
- Mock data from a PLANCK-like CMB measurement, generated according to the procedure of [32]. Note that although we do not use real PLANCK data [40], only synthetic CMB data of comparable constraining power, we shall continue to refer to this synthetic data set as “PLANCK data” when discussing parameter constraints.
- We use also the cosmic shear auto-correlation power spectrum, the galaxy clustering auto-spectrum, and the shear-galaxy cross-correlation power spectrum that will be derived from a EUCLID-like photometric survey. The procedure for generating these mock data sets has already been described in [3]. We assume an exactly known linear galaxy bias for the galaxy clustering power spectrum.

### 6 Forecasting

We now describe our parameter sensitivity forecast for a EUCLID-like photometric survey including a measurement of the cluster mass function. The forecast is based on the construction of a likelihood function for the mock data, whereby the survey’s sensitivities to cosmological parameters can be explored using Bayesian inference techniques.

#### 6.1 Model parameter space

Reference [3] considered a 7-parameter space spanned by the physical baryon density  $\omega_b$ , the physical dark matter (cold dark matter and massive neutrinos) density  $\omega_{\text{dm}}$ , the dimensionless Hubble parameter  $h$ , the amplitude and spectral index of the primordial scalar fluctuations  $A_s$  and  $n_s$ , the reionisation redshift  $z_{\text{re}}$ , and the neutrino density fraction  $f_{\nu} = \omega_{\nu}/\omega_{\text{dm}}$ , with  $\omega_{\nu} = \sum m_{\nu}/(94.1 \text{ eV})$ . In the present analysis we extend this model parameter space to include also the possibility of a non-standard radiation content, quantified by the effective number of massless neutrinos  $N_{\text{eff}}^{\text{ml}}$ , as well as three dynamical dark energy parameters  $\Theta^Q \equiv (w_0, w_a, \hat{c}_s^2)$ , taking the total number of free parameters to eleven:

$$\Theta^{(11)} \equiv (\Theta^{(8)}, \Theta^Q) \equiv \left( (\omega_b, \omega_{\text{dm}}, h, A_s, n_s, z_{\text{re}}, f_{\nu}, N_{\text{eff}}^{\text{ml}}), (w_0, w_a, \hat{c}_s^2) \right). \quad (6.1)$$

As in [3] we assume only one massive neutrino state, so that  $N_{\text{eff}}^{\text{ml}} = 2.046 + \Delta N$ , where  $\Delta N$  parameterises any non-standard physics that may induce a non-standard radiation content. Note that the 0.046 contribution in  $N_{\text{eff}}^{\text{ml}}$  comes from non-instantaneous neutrino decoupling

and finite temperature QED effects, and should in principle be shared between *both* the massless and the massive neutrino states. However, in practice, the precise treatment of this small correction has no measurable effect on our parameter forecast. Lastly, we remark that, parameterised as such,  $\Delta N$  can run from the lowest value of  $-2.046$  to anything positive. Many popular models with non-standard radiation contents associate a positive  $\Delta N$  with additional relativistic particle species such as, e.g., sterile neutrinos [41, 42]. A negative  $\Delta N$  can however arise in, e.g., models with extremely low reheating temperatures [43, 44].

For the non-dark energy part of the parameter space, our fiducial model is defined by the parameter values

$$\Theta_{\text{fid}}^{(8)} = (0.022, 0.1126228, 0.7, 2.1 \times 10^{-9}, 0.96, 11, 0.00553, 2.046). \quad (6.2)$$

For the dark energy sector, we begin with the fiducial values  $\Theta_{\text{fid}}^Q = (-1, 0, \infty)$  corresponding to dark energy in the form of a cosmological constant. The first part of our analysis (up to and including section 7.4) will also be performed with the dark energy sound speed fixed at  $c_s^2 = \infty$ , i.e., homogeneous dark energy. We shall return to dark energy density perturbations in section 7.5, and study the constraints on the dark energy sound speed under a variety of assumptions for the fiducial dark energy parameter values  $\Theta_{\text{fid}}^Q$ .

## 6.2 Likelihood function

Given a theoretical prediction  $N_{\text{th}}$  for the observable number of clusters in a specific redshift and mass bin, the probability of actually observing  $N_{\text{obs}}$  clusters follows a Poisson distribution of  $N_{\text{obs}}$  degrees of freedom. However, the imperfect completeness and efficiency of the survey necessitate that we rescale uncertainty on each data point by an amount  $f^{-1} \equiv \sqrt{[(1/e - 1) + 1/e]/c}$  (see section 5.3). We accomplish this by defining an effective number of observed clusters  $\tilde{N}_{\text{obs}} \equiv f^2 N_{\text{obs}}$ , and likewise an effective theoretical prediction  $\tilde{N}_{\text{th}} \equiv f^2 N_{\text{th}}$ . The effective probability distribution is then

$$\mathcal{L}_P(\tilde{N}_{\text{obs}}|\tilde{N}_{\text{th}}) = \frac{\tilde{N}_{\text{th}}^{\tilde{N}_{\text{obs}}}}{\tilde{N}_{\text{obs}}!} \exp[-\tilde{N}_{\text{th}}]. \quad (6.3)$$

In a real survey, the effective observed number of clusters  $\tilde{N}_{\text{obs}}$  in any one bin is necessarily an integer so that equation (6.3) applies directly. In our forecast, however,  $\tilde{N}_{\text{obs}}$  corresponds to the theoretical expectation value of the fiducial model which generally does not evaluate to an integer. To circumvent this inconvenience, we generalise the likelihood function (6.3) by linearly interpolating the logarithm of the discrete distribution  $\mathcal{L}_P$  in the interval  $[\text{floor}(\tilde{N}_{\text{obs}}), \text{ceiling}(\tilde{N}_{\text{obs}})]$ , i.e.,

$$\begin{aligned} \ln \mathcal{L}(\tilde{N}_{\text{obs}}|\tilde{N}_{\text{th}}) \equiv & \left(1 + \text{floor}(\tilde{N}_{\text{obs}}) - \tilde{N}_{\text{obs}}\right) \ln \mathcal{L}_P(\text{floor}(\tilde{N}_{\text{obs}})|\tilde{N}_{\text{th}}) \\ & + \left(\tilde{N}_{\text{obs}} - \text{floor}(\tilde{N}_{\text{obs}})\right) \ln \mathcal{L}_P(\text{ceiling}(\tilde{N}_{\text{obs}})|\tilde{N}_{\text{th}}). \end{aligned} \quad (6.4)$$

The total cluster log-likelihood function is then obtained straightforwardly by summing  $\ln \mathcal{L}$  over all redshift and mass bins.

## 7 Results

### 7.1 Impact of the number of bins

We examine first how the parameter sensitivities of the cluster survey depend on the number of redshift and mass bins used. Figure 2 shows the posterior standard deviations for a range

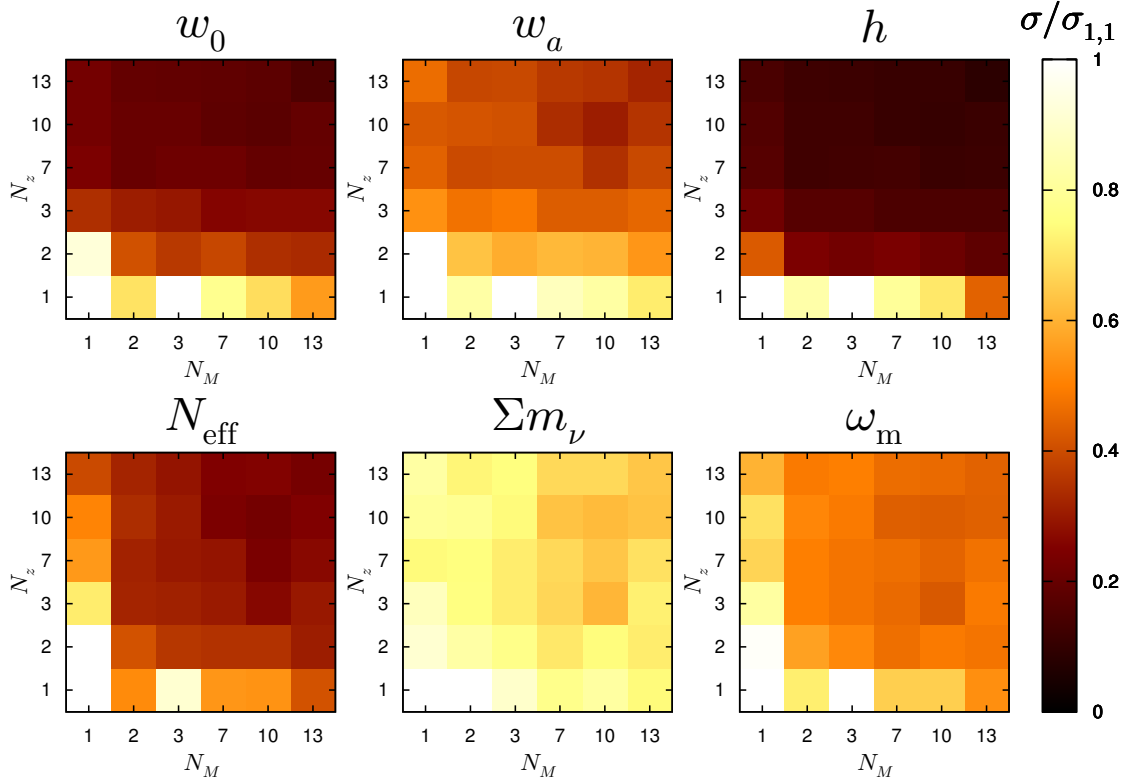


**Figure 2.** Dependence of the posterior standard deviations,  $\sigma$ , for selected cosmological parameters for CMB+clusters on the number of redshift bins  $N_z$  and mass bins  $N_m$ . All numbers have been normalised to the corresponding  $N_z = N_m = 1$  result.

of cosmological parameters derived from a combination of synthetic PLANCK and cluster data as functions of  $N_z$  and  $N_m$ , normalised to the corresponding  $N_z = N_m = 1$  result.

A general trend is immediately clear: for the parameters  $w_0$ ,  $w_a$  and  $h$ , while increasing the number of mass bins results in moderate gain, it is the number of redshift bins used that contributes mostly to improving the parameter sensitivities. For example, in the case of a fixed  $N_z = 1$ , the number of mass bins needs to be increased to 10 or more in order for the sensitivities to improve by 30%, while the same or better sensitivities can be achieved already for a fixed  $N_m = 1$  simply by splitting the data into three redshift bins. For  $N_{\text{eff}}^{\text{ml}}$ ,  $\Sigma m_\nu$  and  $\omega_m$ , the improvements in sensitivity are similar in both directions, and can be traced to the fact that these parameters are primarily responsible for the shape and the overall normalisation of the cluster mass function, less so the redshift dependence. See section 7.2.

Some parameter sensitivities continue to improve beyond  $N_z = 10$  and one might therefore argue for using a very large number of redshift bins. However, for  $N_z = 10$ , the narrowest bin typically has a width of order  $\Delta z = 0.03$ ; pushing much beyond  $N_z = 10$  may cause our results to lose their robustness against redshift uncertainty (see section 4.1). Furthermore, when cluster data are used in conjunction with angular power spectra from cosmic shear and/or galaxy clustering, the gain in going beyond  $N_z = 10$  is substantially reduced. Henceforth, we shall adopt  $N_z = N_m \equiv N_{\text{bin}} = 10$ . Figure 3 shows the marginalised joint two-dimensional posteriors in the  $(w_0, w_a)$ - and the  $(N_{\text{eff}}^{\text{ml}}, \omega_m)$ -subspace from CMB+clusters for this configuration, as well as for  $N_{\text{bin}} = 1, 2$ .

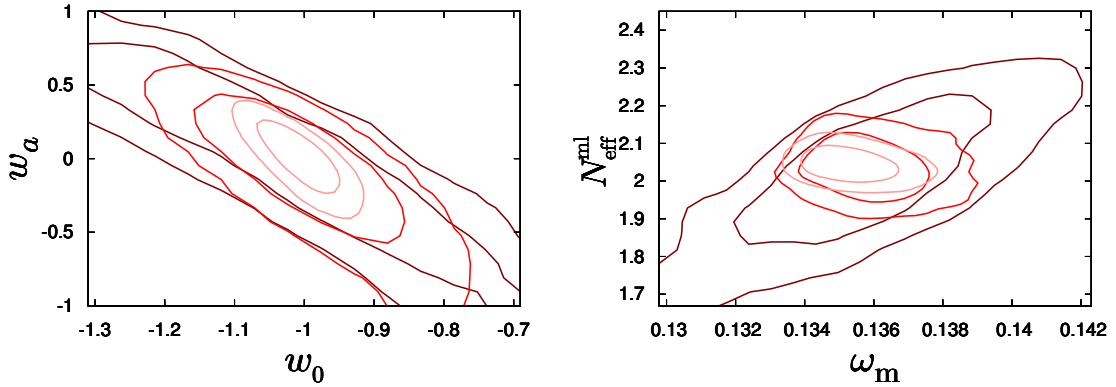


**Figure 3.** Marginalised joint two-dimensional 68% and 95% credible contours from the CMB+clusters data set. The default redshift and mass binning configuration for the cluster data is  $N_{\text{bin}} = 10$  (light red), but we also show the results for  $N_{\text{bin}} = 1$  bin (dark red) and 2 (red).

**Table 1.** Posterior standard deviations for the parameters  $\omega_m$ ,  $h$ ,  $\sum m_\nu$ ,  $N_{\text{eff}}^{\text{ml}}$ ,  $w_0$ , and  $w_a$  derived from various combinations of data sets. Here, “c” denotes PLANCK CMB data, “g” galaxy auto-spectrum (11 redshift bins), “s” shear auto-spectrum (2 bins), “x” shear-galaxy cross-correlation, and “cl” the cluster data (10 redshift bins, 10 mass bins). Also shown is the  $w_0$ - $w_a$  figure-of-merit (FoM), defined in equation (7.1) as  $(\sigma(w_0)\sigma(w_a))^{-1}$ .

Data	$10^3 \times \sigma(\omega_m)$	$100 \times \sigma(h)$	$\sigma(\sum m_\nu)/\text{eV}$	$\sigma(N_{\text{eff}}^{\text{ml}})$	$\sigma(w_0)$	$\sigma(w_a)$	FoM
csgx	1.36	0.858	0.022	0.069	0.077	0.22	59
ccl	1.08	0.323	0.039	0.031	0.038	0.16	165
csgxcl	0.35	0.231	0.0098	0.019	0.025	0.085	454

## 7.2 Probes of the expansion history versus probes of the power spectrum

The main advantage of the cluster mass function (with redshift binning) over the shear and the galaxy power spectra is that it is highly sensitive to those parameters that govern the linear growth function and hence (in the case of standard gravity) the expansion history of the universe. This makes redshift-binned cluster measurements especially powerful for constraining dark energy parameters, as well as for establishing the reduced matter density  $\Omega_m \equiv \omega_m/h^2$ . Furthermore, because the normalisation of the cluster abundance is directly sensitive to the physical matter density  $\omega_m$ , the Hubble parameter  $h$  can also be very effectively constrained. As shown in table 1 and figure 4, CMB+clusters (“ccl”) performs up to a factor of two better than CMB+shear+galaxies (“csgx”) when it comes to placing constraints on  $w_0$ ,  $w_a$ ,  $\omega_m$ , and  $h$ .

In contrast, the sum of neutrino masses  $\sum m_\nu$  is significantly less well measured by clusters than by the shear and the galaxy power spectra. This is because firstly,  $\sum m_\nu$  plays a negligible role (compared with, e.g., dark energy parameters) in the redshift dependence of the late-time linear growth function. Secondly, although the shape of the cluster mass function is in principle also subject to a mass-dependent suppression due to neutrino free-streaming (e.g., [45, 46]), the actual range of cluster masses probed by a realistic cluster survey is very narrow (see figure 1), so that the suppression can be easily mimicked by other effects such as an excess of relativistic energy density or simply a smaller initial

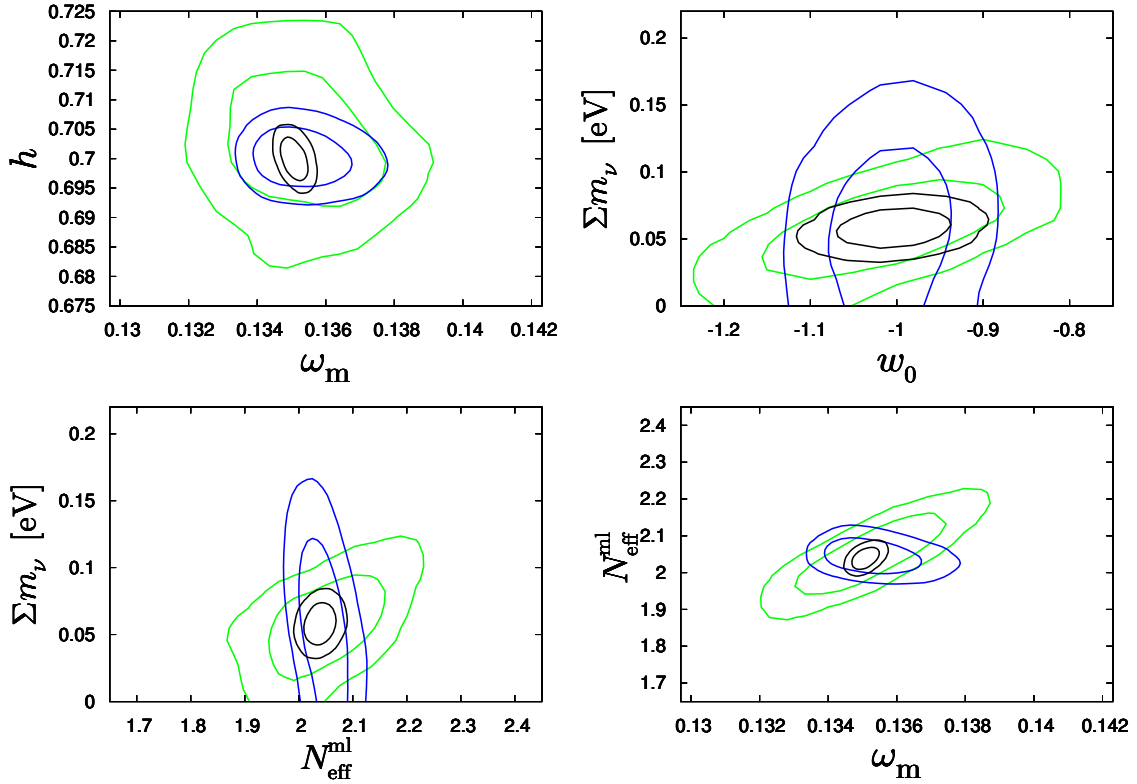


**Figure 4.** Marginalised joint two-dimensional 68% and 95% credible contours from the CMB+clusters data set (“ccl”, blue), CMB+shear+galaxies (“csgx”, green), and all data sets (“csgxcl”, black) for various parameters, using the default binning configuration of  $N_{\text{bin}} = 10$  for the cluster data.

fluctuation amplitude.

Interestingly, a non-standard radiation content as parameterised by  $N_{\text{eff}}^{\text{ml}}$ , although it has no direct effect on the late-time expansion or growth history, is exceptionally well constrained by CMB+clusters. This can be understood as follows: using CMB data alone,  $N_{\text{eff}}^{\text{ml}}$  is strongly degenerate with  $\omega_m$  and  $h$ . However, because the cluster mass function is directly sensitive to  $\omega_m$  and  $h$ , it very effectively lifts any degeneracy of these parameters with  $N_{\text{eff}}^{\text{ml}}$  when used in combination with CMB data. As shown in the lower right panel of figure 4, very little degeneracy remains between  $N_{\text{eff}}^{\text{ml}}$  and  $\omega_m$  for the CMB+clusters data set. A more telling illustration of how the binned cluster data removes the  $(N_{\text{eff}}, \omega_m)$ -degeneracy can be found in the right panel of figure 3: Here, when only one redshift and mass bin is used, the cluster mass function is primarily sensitive to the fluctuation amplitude on small scales so that the  $(N_{\text{eff}}, \omega_m)$ -degeneracy persists in the CMB+clusters fit. However, as soon as access to the linear growth function and some shape information become available through as little as  $N_z = N_m = 2$  bins, the degeneracy becomes broken because of the growth function’s direct dependence on  $\Omega_m$  and of the normalisation’s dependence on  $\omega_m$ .

### 7.3 Combining all data sets: constraints on neutrino parameters

Perhaps the most noteworthy result of table 1 is that, while CMB+shear+galaxies (“csgx”) and CMB+clusters (“ccl”) are well-suited to measuring different parameters and are hence in a sense complementary to each other, the combined usage of *all* data sets, i.e., the “csgxcl”

combination, always leads to significant enhancements in *all* parameter sensitivities. This result can be understood from figure 4, where it is clear that the ‘csgx’ and ‘ccl’ datasets give rise to almost orthogonal parameter degeneracy directions. In combination these data sets conspire to lift each other’s degeneracies.

For neutrino parameters, it is interesting to note that while ‘csgx’ and ‘ccl’ return  $\sigma(\sum m_\nu) = 0.022$  eV and 0.039 eV respectively, in combination the sensitivity improves to  $\sigma(\sum m_\nu) = 0.0098$  eV. This is as good a sensitivity as was found earlier in [3] from the ‘csgx’ data set, but for a much simpler 7-parameter cosmological model. Thus, we again conclude that EUCLID, in combination with PLANCK CMB data, will be able to probe neutrino masses at  $5\sigma$  precision or better. Likewise, the ‘csgxcl’ data set is now sensitive to  $N_{\text{eff}}^{\text{ml}}$  at  $\sigma(N_{\text{eff}}^{\text{ml}}) = 0.019$ , meaning that for the first time the small deviation of 0.046 from 3 in the fiducial  $N_{\text{eff}}^{\text{ml}}$  can be probed with  $2\sigma$  precision.

#### 7.4 The dark energy figure-of-merit

It is useful to quantify the constraining power of an observation (or a combination of observations) in terms of a figure-of-merit (FoM). Here, we define a dark energy FoM,

$$\text{FoM} \equiv (\sigma(w_0)\sigma(w_a))^{-1}, \quad (7.1)$$

which is simply the reciprocal of the product of the posterior standard deviations for  $w_0$  and  $w_a$ , so that the larger the FoM the better the constraining power.

To relate our FoM to that adopted in the EUCLID Red Book [2], we note that the latter is defined as  $\text{FoM} \equiv (\sigma(w_p)\sigma(w_a))^{-1}$ , following from a parameterisation of the dynamical dark energy equation of state of the form  $w(a) = w_p + w_a(a_p - a)$ , where the ‘pivot’ scale factor  $a_p$  is chosen such that the uncertainties on  $w_p$  and  $w_a$  are uncorrelated. Our parameterisation (equation (2.1)) corresponds to setting  $a_p = 1$ . The two parameterisations of  $w(a)$  are in principle equivalent in the sense that the areas of the resulting error ellipses in the  $(w_0, w_a)$ - and  $(w_p, w_a)$ -subspaces are the same [47]. In the case of the  $(w_p, w_a)$ -parameterisation, because of the absence of correlations the product  $\sigma(w_p)\sigma(w_a)$  represents a reasonable estimate of area of the 68%-credible region. In our  $(w_0, w_a)$ -parameterisation, however, strong correlations exist between  $w_0$  and  $w_a$ , as is evident in figure 3, such that the product  $\sigma(w_0)\sigma(w_a)$  *always overestimates* the area of the error ellipse. It follows that

$$(\sigma(w_0)\sigma(w_a))^{-1} \leq (\sigma(w_p)\sigma(w_a))^{-1}, \quad (7.2)$$

i.e., our FoM defined in equation (7.1) is conservative in comparison with that of [2].

The FoMs for various fiducial models and combinations of data sets are presented in table 2, where it is immediately clear that the EUCLID science objective of reaching a FoM in excess of 400 in the context of the  $\Lambda$ CDM model can be realised using the ‘csgxcl’ data combination. We note that this number is formally much smaller than the estimate of 4000 quoted in [2]. This can be traced to (a) the conservative nature of our FoM definition, (b) the larger parameter space used in our analysis (constraints on  $w_p$  and  $w_a$  quoted in [2] have been obtained assuming fixed values of  $\sum m_\nu = 0$  eV and  $N_{\text{eff}}^{\text{ml}} = 3.046$ ), and (c) the Fisher matrix approach adopted in the analysis of [2], which tends to predict constraints that are too stringent compared with those from a Monte Carlo analysis—the recent analysis of [48], for example, found a factor of 2 to 3 overestimation of the sensitivity of future cluster surveys to  $w_0$  and  $w_a$ .

Lastly, we note that for a given data set combination, there are some variations in the sensitivities to  $w_0$  and  $w_a$  (especially the latter) depending on our choice of fiducial model.



**Table 2.** Posterior standard deviations for the parameters  $w_0$  and  $w_a$  in various fiducial models derived from various data set combinations. See legend in table 1. Also shown is the  $w_0$ - $w_a$  figure-of-merit (FoM).

Data	$w_0$	$w_a$	$\sigma(w_0)$	$\sigma(w_a)$	FoM
ccl	-1.00	0.00	0.038	0.16	165
ccl	-0.83	0.00	0.036	0.13	212
ccl	-1.17	0.00	0.037	0.20	133
ccl	-1.00	0.35	0.030	0.14	231
ccl	-1.00	-0.35	0.041	0.22	109
csgxcl	-1.00	0.00	0.025	0.085	454
csgxcl	-0.83	0.00	0.022	0.070	645
csgxcl	-1.17	0.00	0.024	0.083	496
csgxcl	-1.00	0.35	0.022	0.070	658
csgxcl	-1.00	-0.35	0.025	0.086	470

The FoM likewise varies by up to 40% away from the  $\Lambda$ CDM value. However, these variations across fiducial models for the same data combination are typically minor compared with the variations across *different* data combinations for the same fiducial model. Thus, by and large, results for the  $\Lambda$ CDM model can be treated as representative.

## 7.5 Dark energy sound speed and perturbations

In the analysis so far we have neglected the effect of dark energy perturbations. We now introduce dark energy perturbations into the analysis as per the discussion in section 2, and investigate the constraining power of a EUCLID-like survey on this aspect of dark energy.

We consider four fiducial models differing in their fiducial values of  $(w_0, w_a, \hat{c}_s^2)$ :

- Model 1:  $(w_0, w_a) = (-1, 0)$  and  $\hat{c}_s^2 = 1$ <sup>1</sup> (i.e.,  $\Lambda$ CDM)
- Model 2:  $(w_0, w_a) = (-1.17, 0)$  and  $\hat{c}_s^2 = 1$
- Model 3:  $(w_0, w_a) = (-0.83, 0)$  and  $\hat{c}_s^2 = 1$
- Model 4:  $(w_0, w_a) = (-0.83, 0)$  and  $\hat{c}_s^2 = 10^{-6}$

In all models, we fix  $w_a = 0$  because of the pathological behaviour of dark energy perturbations when crossing the phantom divide  $w = -1$  [49]. We present only results obtained from the “csgxcl” data sets, shown in table 3 and figure 5. All results have been obtained assuming a top-hat prior on  $\log \hat{c}_s^2$  of  $\log \hat{c}_s^2 \in [-10, 2]$ . Note that the posteriors for  $\log \hat{c}_s^2$  in some models clearly show no peak structure so that  $\log \hat{c}_s^2$  can only be constrained from one side. In such cases, instead of the posterior standard deviation, we quote in table 3 the appropriate one-sided limits.

For the three models with  $\hat{c}_s^2 = 1$ , the Jeans mass  $M_J$ , defined in equation (A.6), is of order  $10^{23} M_\odot$  at  $z = 0$  and lies well above the maximum observed cluster mass  $M_{\text{high}}$ . This tells us immediately that these models are undetectable by a EUCLID-like cluster survey. However, as  $\hat{c}_s^2$  drops below  $\sim 10^{-2}$  ( $M_J \sim 10^{20} M_\odot$ ), the additional mass-dependence it produces on the cluster mass function begins to be visible to EUCLID, and we see a sharp

<sup>1</sup>The choice of  $\hat{c}_s^2$  for the  $\Lambda$ CDM model is immaterial, since by definition dark energy does not cluster in this model and  $\delta_Q = 0$  is automatically implemented in CAMB.

**Table 3.** Posterior standard deviations for  $w_0$  and  $\log \hat{c}_s^2$  in various fiducial models derived from the combined “csgxcl” data set. See legend in table 1. In those cases where  $\log \hat{c}_s^2$  can only be constrained from one side, we quote the corresponding 68% (95%) credible limits.

Data	$w_0$	$w_a$ (fixed)	$\hat{c}_s^2$	$\log \hat{c}_s^2$	$\sigma(w_0)$	$\sigma(\log \hat{c}_s^2)$
csgxcl	-1.00	0.00	1	0	0.0051	unconstrained
csgxcl	-0.83	0.00	1	0	0.0048	$> -1.8(-4.2)$
csgxcl	-0.83	0.00	$10^{-6}$	-6	0.0047	0.13
csgxcl	-1.17	0.00	1	0	0.0061	$> -1.8(-3.9)$

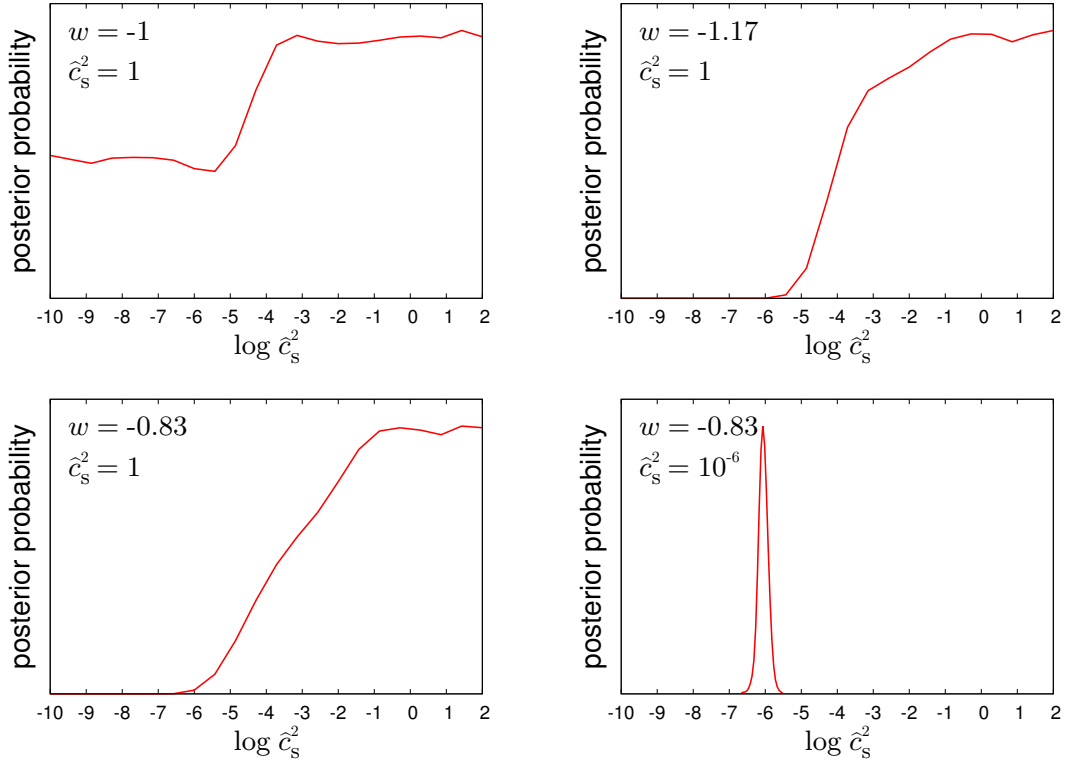


**Figure 5.** Marginalised one-dimensional posterior probability density for  $\log \hat{c}_s^2$  for four different fiducial models (see labels in plots) from a “csgxcl” fit.

decrease in the posterior probability for  $\log \hat{c}_s^2$  in figure 5. In the case of models 2 and 3 (which have  $w_0 = -0.83, -1.17$ ), the corresponding posterior probabilities eventually drop to zero, thus allowing us to place a lower limit on  $\hat{c}_s^2$ :  $\log \hat{c}_s^2 > -4.0$  (95% C.I.). No constraints on  $\hat{c}_s^2$  are however available for model 1 (the  $\Lambda$ CDM model), because dark energy perturbations are generally suppressed by a factor of  $1 + w_0$  relative to dark matter perturbations and are hence practically nonexistent in the vicinity of  $w_0 = -1$ .

The remaining model 4 with  $\hat{c}_s^2 = 10^{-6}$  has a remarkably well-constrained dark energy sound speed,  $\sigma(\log \hat{c}_s^2) = 0.13$ . This is a consequence of  $M_J$  ( $\simeq 4 \times 10^{14} M_\odot$  at  $z = 0$ ) lying within the cluster mass range probed by EUCLID, so that the transition from minimal dark energy clustering to full dark energy clustering can be very effectively observed with the help of cluster mass binning. We emphasise however that our choice of the fiducial value of

$w_0 = -0.83$  also plays a crucial role towards establishing this remarkable sensitivity, again because of the  $1 + w_0$  suppression suffered by the dark energy perturbations relative to the dark matter perturbations.

## 8 Conclusions

In this paper we have considered the constraining power of a EUCLID-like galaxy survey on cosmological parameters in conjunction with PLANCK CMB data. This study is an extension of our previous investigation in [3], in that we have included in the present analysis mock data from the EUCLID cluster survey in addition to the angular cosmic shear and galaxy power spectra expected from the photometric redshift survey, and we have expanded the parameter space to encompass also dynamical dark energy as well as the possibility of (small-scale) dark energy perturbations.

We find that, comparing CMB+clusters and CMB+shear+galaxies, the former has up to a factor of two better sensitivities for those parameters that affect only the late-time growth and expansion history of the universe, i.e., those parameters that determine the dynamical dark energy equation of state, and the Hubble parameter. This improvement arises chiefly from our adoption of redshift binning for the observed clusters, which allows us in particular to probe the transition from matter to dark energy domination. Neutrino masses, on the other hand, are not particularly well-constrained by CMB+clusters ( $\sigma(\sum m_\nu) = 0.039$  eV in a 10-parameter model), clearly because they do not play a major role in the overall linear growth of matter density perturbations. Importantly, however, the degeneracy directions of CMB+clusters and CMB+shear+galaxies are largely orthogonal. This means that even though neither data set performs particularly impressively for any one cosmological parameter, in combination they help to lift each other's degeneracies. The sensitivities to  $\sum m_\nu$  from CMB+shear+galaxies+clusters is, for example,  $\sigma(\sum m_\nu) = 0.0098$  eV in a 10-parameter model, which is as good as that obtained previously in [3] from CMB+shear+galaxies for a much simpler 7-parameter  $\Lambda$ CDM model. Thus, we can conclude again that a EUCLID-like survey has the potential to measure neutrino masses at  $5\sigma$  precision or more.

For the dark energy parameters, we find that the combination of CMB+shear+galaxies+clusters results in a dark energy figure-of-merit (FoM), defined in this work as  $(\sigma(w_0)\sigma(w_a))^{-1}$ , of 454 for a  $\Lambda$ CDM fiducial cosmology, with upward variations of up to 45% for fiducial cosmologies in which  $w_0 \neq -1$  and  $w_a \neq 0$ . Although this number is clearly sufficient to meet the EUCLID science objective of reaching an FoM beyond 400, we note that it is significantly smaller than the estimate of 4000 quoted in the EUCLID Red Book [2]. This discrepancy can be traced to our more conservative definition of the FoM, as well as the smaller parameter space and the Fisher matrix forecast method (which tends to be too optimistic compared with a Monte Carlo forecast) adopted in the analysis of [2].

Finally, we investigate the detectability of dark energy perturbations, parameterised in terms of a non-adiabatic fluid sound speed  $\hat{c}_s^2$ . Along the way we also introduce a model of the cluster mass function that incorporates the effects of  $\hat{c}_s^2$  based on solving and interpolating the spherical top-hat collapse in the known limits of  $\hat{c}_s^2 \rightarrow \infty$  (homogeneous dark energy) and  $\hat{c}_s^2 = 0$  (dark energy comoving with nonrelativistic matter). We find that for values of the dark energy sound speed whereby the associated Jeans mass lies within the mass detection range of the cluster survey, dark energy perturbations imprint a distinct step-like signature in the observed cluster mass function. With the help of cluster mass binning, this signature makes these models distinguishable from those in which the Jeans mass lies well outside (both

below and above) the detection range. Indeed, using 10 mass bins per redshift bin, we find that  $\log \hat{c}_s^2$  can be measured to a  $1\sigma$  precision of 0.13 in these models, as long as the fiducial value of  $w_0$  deviates from  $-1$  by as much as is presently allowed by observations.

**Note added:** As this work was in its final stage of completion, we learnt of the investigation of [50] which considered the EUCLID cluster survey’s sensitivities to neutrino parameters. While a full comparison is difficult because of the generally different assumptions about the survey parameters and the model parameter space, where the assumptions do to some extent coincide the two analyses appear to be compatible.

## Acknowledgements

We acknowledge computing resources from the Danish Center for Scientific Computing (DCSC). OEB acknowledges support from the Stellar Astrophysics Centre at Aarhus University.

## A Interpolating the spherical collapse between the two limits of $\hat{c}_s^2$

The spherical top-hat collapse model is exactly defined only in the limits  $\hat{c}_s^2 \rightarrow \infty$  and  $\hat{c}_s^2 = 0$ . In the first case, the dark energy component is non-clustering. The dark matter and baryon components alone suffer gravitational collapse, so that the overdense region preserves its top-hat density profile throughout the collapse, with a comoving radius  $X$  given by

$$\frac{\ddot{X}}{X} + \mathcal{H} \frac{\dot{X}}{X} = -4\pi G a^2 \bar{\rho}_m \delta_m, \quad (\text{A.1})$$

where

$$\delta_m(\tau) = [1 + \delta_m(\tau_i)] \left[ \frac{X(\tau_i)}{X(\tau)} \right]^3 - 1 \quad (\text{A.2})$$

follows from conservation of the total mass of nonrelativistic matter  $M_m$  in the top-hat region. The virial radius  $R_{\text{vir}}$ , defined as the physical radius of the top-hat at the moment the collapsing region fulfils the virial theorem, is as usual one half of physical radius at turnaround, and the virial mass  $M_{\text{vir}}$  is identical to  $M_m$ , which we also equate with the mass of the cluster  $M$ .

In the second case, an exactly vanishing non-adiabatic dark energy sound speed means that, like nonrelativistic matter, dark energy density perturbations also evolve identically on all scales. This again leads to the preservation of the top-hat density profile and hence the conservation of  $M_m$  in the region defined by the comoving radius  $X$ , now determined by

$$\frac{\ddot{X}}{X} + \mathcal{H} \frac{\dot{X}}{X} = -4\pi G a^2 [\bar{\rho}_m \delta_m + \bar{\rho}_Q \delta_Q]. \quad (\text{A.3})$$

A conservation law can likewise be written down for the clustered dark energy component

$$\dot{\rho}_Q + 3 \left( \mathcal{H} + \frac{\dot{X}}{X} \right) (\rho_Q + \bar{P}_Q) = 0, \quad (\text{A.4})$$

where  $\rho_Q$  denotes the dark energy density in the top-hat region. We assume that at any one time the clustered dark energy contributes a mass [28]

$$M_Q(\tau) \equiv \frac{4\pi}{3} \bar{\rho}_Q(\tau) \delta_Q(\tau) [a(\tau) X(\tau)]^3 \quad (\text{A.5})$$

to the total mass of the system. This clustered dark energy takes part in virialisation, defined here as the instant the system satisfies the condition  $d^2I/dt^2 = 0$ , where  $I \equiv (2/5)(M_m + M_Q)(aX)^2$  is the top-hat's moment of inertia, and  $t$  is the cosmic time ( $dt = a d\tau$ ). The physical radius of the top-hat at this instant is the virial radius  $R_{\text{vir}} \equiv aX(\tau_{\text{vir}})$ , and the total mass the virial mass  $M_{\text{vir}} \equiv M_m + M_Q(\tau_{\text{vir}})$ . Linearised forms of equations (A.1) to (A.4) can be found in references [9, 28].

Between the two limits, any finite nonvanishing  $\hat{c}_s^2$  necessarily causes the overdense region to evolve away from the top-hat configuration and to become ill-defined. The absence of strict conservation laws in this intermediate regime also renders the system not readily soluble. Nonetheless, the transition between the two known limits have been investigated using a quasi-linear approach in [9, 29], where it was found that, for a fixed  $\hat{c}_s^2$  and at a given collapse redshift  $z$ , the transition generically results in a step-like feature in the linear threshold density  $\delta_c$ , as well as in the quantities  $\Delta_{\text{vir}} \equiv 3M_m/4\pi\bar{\rho}_m(\tau_{\text{vir}})R_{\text{vir}}^3$  and  $\eta_{\text{vir}} \equiv M_Q(\tau_{\text{vir}})/M_m$ , as  $M_m$  is varied from  $M_m \ll M_J$  to  $M_m \gg M_J$ , with

$$\begin{aligned} M_J(a) &\equiv \frac{4\pi}{3}\bar{\rho}_m(a) \left[ \frac{a\lambda_J(a)}{2} \right]^3 \\ &= 9.7 \times 10^{23} c_s^3 \Omega_m a^{-3} \left( \Omega_m a^{-3} + \Omega_Q e^{-3 \int_0^a da' [1+w(a')]/a'} \right)^{-3/2} h^{-1} M_\odot \quad (\text{A.6}) \end{aligned}$$

denoting the Jeans mass, and  $\lambda_J \equiv 2\pi\hat{c}_s/\mathcal{H}$  the corresponding comoving Jeans length.

To incorporate this feature in the cluster mass function for our MCMC analysis, our strategy is as follows.

1. For each given set of cosmological parameters, we solve the spherical collapse model for  $\delta_c$ ,  $\Delta_{\text{vir}}$ , and  $\eta_{\text{vir}}$  in the two limits of  $\hat{c}_s^2$  using equations (A.1) to (A.4) as functions of the collapse redshift  $z$ .
2. At each redshift, we interpolate the two limits using the formulae

$$\delta_c(M_m) = \Delta(\delta_c^\infty, \delta_c^0) \tanh \left[ A_1 \left( \log M_m - \log \frac{M_J}{B_1} \right) \right] + \Sigma(\delta_c^\infty, \delta_c^0), \quad (\text{A.7})$$

$$\Delta_{\text{vir}}(M_m) = \Delta(\Delta_{\text{vir}}^\infty, \Delta_{\text{vir}}^0) \tanh \left[ A_2 \left( \log M_m - \log \frac{M_J}{B_2} \right) \right] + \Sigma(\Delta_{\text{vir}}^\infty, \Delta_{\text{vir}}^0), \quad (\text{A.8})$$

$$\eta_{\text{vir}}(M_m) = \Delta(\eta_{\text{vir}}^\infty, \eta_{\text{vir}}^0) \tanh \left[ A_3 \left( \log M_m - \log \frac{M_J}{B_3} \right) \right] + \Sigma(\eta_{\text{vir}}^\infty, \eta_{\text{vir}}^0), \quad (\text{A.9})$$

where  $x^\infty$  denotes the value of  $x = \delta_c, \Delta_{\text{vir}}, \eta_{\text{vir}}$  in the  $\hat{c}_s^2 \rightarrow \infty$  limit,  $x^0$  the  $\hat{c}_s^2 = 0$  limit, and  $\Delta(x^\infty, x^0) \equiv (x^\infty - x^0)/2$  and  $\Sigma(x^\infty, x^0) \equiv (x^\infty + x^0)/2$  represent their difference and sum respectively. The parameters  $A_{1,2,3}$  and  $B_{1,2,3}$  are fitting coefficients, adjusted to fit respectively the sharpness and location of the transition. At  $z = 0$  and for  $(w_0, w_a) = (-0.8, 0)$ , we find that  $A_{1,2,3} \simeq 1.4$ , and  $B_{1,2,3} \simeq 20$  reproduce the quasi-linear results of [9, 29] in the region immediately below the Jeans mass quite well. For simplicity, we adopt these parameter values for all redshifts and cosmological models.

3. Lastly, we identify the virial mass with the cluster mass, i.e.,  $M_{\text{vir}} \equiv M$ , and construct the functions  $\delta_c(M, z)$  and  $R_{\text{vir}}(M, z)$  according to

$$\delta_c(M, z) \equiv \delta_c(M_{\text{vir}}(M_m), z) \equiv \delta_c(M_m, z), \quad (\text{A.10})$$

$$R_{\text{vir}}(M, z) \equiv R_{\text{vir}}(M_{\text{vir}}(M_m), z) \equiv R_{\text{vir}}(M_m, z), \quad (\text{A.11})$$

which are used in sections 3.1 and 5.1 determine the cluster mass function and the mass detection threshold, respectively.

## References

- [1] **LSST Science Collaborations, LSST Project** Collaboration, P. A. Abell *et al.*, “LSST Science Book, Version 2.0,” [arXiv:0912.0201](#) [[astro-ph.IM](#)].
- [2] R. Laureijs, J. Amiaux, S. Arduini, J.-L. Augeres, J. Brinchmann, *et al.*, “Euclid Definition Study Report,” [arXiv:1110.3193](#) [[astro-ph.CO](#)].
- [3] J. Hamann, S. Hannestad, and Y. Y. Y. Wong, “Measuring neutrino masses with a future galaxy survey,” *JCAP* **1211** (2012) 052, [arXiv:1209.1043](#) [[astro-ph.CO](#)].
- [4] **Planck** Collaboration, “The scientific programme of Planck,” [arXiv:astro-ph/0604069](#) [[astro-ph](#)].
- [5] M. Chevallier and D. Polarski, “Accelerating universes with scaling dark matter,” *Int.J.Mod.Phys. D* **10** (2001) 213–224, [arXiv:gr-qc/0009008](#) [[gr-qc](#)].
- [6] E. V. Linder, “Exploring the expansion history of the universe,” *Phys.Rev.Lett.* **90** (2003) 091301, [arXiv:astro-ph/0208512](#) [[astro-ph](#)].
- [7] A. Pavlov, L. Samushia, and B. Ratra, “Forecasting cosmological parameter constraints from near-future space-based galaxy surveys,” *Astrophys.J.* **760** (2012) 19, [arXiv:1206.3123](#) [[astro-ph.CO](#)].
- [8] G. Ballesteros and J. Lesgourgues, “Dark energy with non-adiabatic sound speed: initial conditions and detectability,” *JCAP* **1010** (2010) 014, [arXiv:1004.5509](#) [[astro-ph.CO](#)].
- [9] T. Basse, O. E. Bjælde, and Y. Y. Y. Wong, “Spherical collapse of dark energy with an arbitrary sound speed,” *JCAP* **1110** (2011) 038, [arXiv:1009.0010](#) [[astro-ph.CO](#)].
- [10] S. DeDeo, R. Caldwell, and P. J. Steinhardt, “Effects of the sound speed of quintessence on the microwave background and large scale structure,” *Phys.Rev. D* **67** (2003) 103509, [arXiv:astro-ph/0301284](#) [[astro-ph](#)].
- [11] R. Bean and O. Doré, “Probing dark energy perturbations: The Dark energy equation of state and speed of sound as measured by WMAP,” *Phys.Rev. D* **69** (2004) 083503, [arXiv:astro-ph/0307100](#) [[astro-ph](#)].
- [12] J. Weller and A. Lewis, “Large scale cosmic microwave background anisotropies and dark energy,” *Mon.Not.Roy.Astron.Soc.* **346** (2003) 987–993, [arXiv:astro-ph/0307104](#) [[astro-ph](#)].
- [13] S. Wang, J. Khoury, Z. Haiman, and M. May, “Constraining the evolution of dark energy with a combination of galaxy cluster observables,” *Phys.Rev. D* **70** (2004) 123008, [arXiv:astro-ph/0406331](#) [[astro-ph](#)].
- [14] M. Takada and S. Bridle, “Probing dark energy with cluster counts and cosmic shear power spectra: including the full covariance,” *New J.Phys.* **9** (2007) 446, [arXiv:0705.0163](#) [[astro-ph](#)].
- [15] E. Sefusatti, C. Vale, K. Kadota, and J. Frieman, “Primordial non-Gaussianity and Dark Energy constraints from Cluster Surveys,” *Astrophys.J.* **658** (2007) 669–679, [arXiv:astro-ph/0609124](#) [[astro-ph](#)].
- [16] S. Wang, Z. Haiman, W. Hu, J. Khoury, and M. May, “Weighing neutrinos with galaxy cluster surveys,” *Phys.Rev.Lett.* **95** (2005) 011302, [arXiv:astro-ph/0505390](#) [[astro-ph](#)].
- [17] M. Lima and W. Hu, “Self-calibration of cluster dark energy studies: Observable-mass distribution,” *Phys.Rev. D* **72** (2005) 043006, [arXiv:astro-ph/0503363](#) [[astro-ph](#)].

- [18] L. R. Abramo, R. C. Batista, and R. Rosenfeld, “The signature of dark energy perturbations in galaxy cluster surveys,” *JCAP* **0907** (2009) 040, [arXiv:0902.3226 \[astro-ph.CO\]](#).
- [19] R. K. Sheth and G. Tormen, “Large scale bias and the peak background split,” *Mon.Not.Roy.Astron.Soc.* **308** (1999) 119, [arXiv:astro-ph/9901122 \[astro-ph\]](#).
- [20] A. Jenkins, C. Frenk, S. D. White, J. Colberg, S. Cole, *et al.*, “The Mass function of dark matter halos,” *Mon.Not.Roy.Astron.Soc.* **321** (2001) 372, [arXiv:astro-ph/0005260 \[astro-ph\]](#).
- [21] J. L. Tinker, A. V. Kravtsov, A. Klypin, K. Abazajian, M. S. Warren, *et al.*, “Toward a halo mass function for precision cosmology: The Limits of universality,” *Astrophys.J.* **688** (2008) 709–728, [arXiv:0803.2706 \[astro-ph\]](#).
- [22] A. Lewis, A. Challinor, and A. Lasenby, “Efficient computation of CMB anisotropies in closed FRW models,” *Astrophys.J.* **538** (2000) 473–476, [arXiv:astro-ph/9911177 \[astro-ph\]](#).
- [23] D. Mota and C. van de Bruck, “On the Spherical collapse model in dark energy cosmologies,” *Astron.Astrophys.* **421** (2004) 71–81, [arXiv:astro-ph/0401504 \[astro-ph\]](#).
- [24] J. E. Gunn and I. Gott, J. Richard, “On the Infall of Matter into Clusters of Galaxies and Some Effects on Their Evolution,” *Astrophys.J.* **176** (1972) 1–19.
- [25] L.-M. Wang and P. J. Steinhardt, “Cluster abundance constraints on quintessence models,” *Astrophys.J.* **508** (1998) 483–490, [arXiv:astro-ph/9804015 \[astro-ph\]](#).
- [26] A. Cooray and R. K. Sheth, “Halo models of large scale structure,” *Phys.Rept.* **372** (2002) 1–129, [arXiv:astro-ph/0206508 \[astro-ph\]](#).
- [27] L. Abramo, R. Batista, L. Liberato, and R. Rosenfeld, “Structure formation in the presence of dark energy perturbations,” *JCAP* **0711** (2007) 012, [arXiv:0707.2882 \[astro-ph\]](#).
- [28] P. Creminelli, G. D’Amico, J. Norena, L. Senatore, and F. Vernizzi, “Spherical collapse in quintessence models with zero speed of sound,” *JCAP* **1003** (2010) 027, [arXiv:0911.2701 \[astro-ph.CO\]](#).
- [29] T. Basse, O. E. Bjælde, S. Hannestad, and Y. Y. Y. Wong, “Confronting the sound speed of dark energy with future cluster surveys,” [arXiv:1205.0548 \[astro-ph.CO\]](#).
- [30] Y. M. Bahe, I. G. McCarthy, and L. J. King, “Mock weak lensing analysis of simulated galaxy clusters: bias and scatter in mass and concentration,” *Mon.Not.Roy.Astron.Soc.* **421** (2012) 1073–1088, [arXiv:1106.2046 \[astro-ph.CO\]](#).
- [31] M. R. Becker and A. V. Kravtsov, “On the Accuracy of Weak Lensing Cluster Mass Reconstructions,” *Astrophys.J.* **740** (2011) 25, [arXiv:1011.1681 \[astro-ph.CO\]](#).
- [32] L. Perotto, J. Lesgourgues, S. Hannestad, H. Tu, and Y. Y. Y. Wong, “Probing cosmological parameters with the CMB: Forecasts from full Monte Carlo simulations,” *JCAP* **0610** (2006) 013, [arXiv:astro-ph/0606227 \[astro-ph\]](#).
- [33] T. Hamana, M. Takada, and N. Yoshida, “Searching for massive clusters in weak lensing surveys,” *Mon.Not.Roy.Astron.Soc.* **350** (2004) 893, [arXiv:astro-ph/0310607 \[astro-ph\]](#).
- [34] J. F. Navarro, C. S. Frenk, and S. D. White, “The Structure of cold dark matter halos,” *Astrophys.J.* **462** (1996) 563–575, [arXiv:astro-ph/9508025 \[astro-ph\]](#).
- [35] L. Van Waerbeke, “Noise properties of gravitational lens mass reconstruction,” *Mon.Not.Roy.Astron.Soc.* **313** (2000) 524–532, [arXiv:astro-ph/9909160 \[astro-ph\]](#).
- [36] J. F. Hennawi and D. N. Spergel, “Mass selected cluster cosmology. 1: Tomography and optimal filtering,” *Astrophys.J.* (2004) , [arXiv:astro-ph/0404349 \[astro-ph\]](#).
- [37] M. J. White, L. van Waerbeke, and J. Mackey, “Completeness in weak lensing searches for clusters,” *Astrophys.J.* **575** (2002) 640–649, [arXiv:astro-ph/0111490 \[astro-ph\]](#).



- [38] F. Feroz, P. Marshall, and M. Hobson, “Cluster detection in weak lensing surveys,” [arXiv:0810.0781 \[astro-ph\]](#).
- [39] F. Pace, M. Maturi, M. Meneghetti, M. Bartelmann, L. Moscardini, *et al.*, “Testing the reliability of weak lensing cluster detections,” [arXiv:astro-ph/0702031 \[ASTRO-PH\]](#).
- [40] **Planck Collaboration** Collaboration, P. Ade *et al.*, “Planck 2013 results. I. Overview of products and scientific results,” [arXiv:1303.5062 \[astro-ph.CO\]](#).
- [41] R. Barbieri and A. Dolgov, “Neutrino oscillations in the early universe,” *Nucl.Phys.* **B349** (1991) 743–753.
- [42] K. Kainulainen, “Light singlet neutrinos and the primordial nucleosynthesis,” *Phys.Lett.* **B244** (1990) 191–195.
- [43] M. Kawasaki, K. Kohri, and N. Sugiyama, “MeV scale reheating temperature and thermalization of neutrino background,” *Phys.Rev.* **D62** (2000) 023506, [arXiv:astro-ph/0002127 \[astro-ph\]](#).
- [44] S. Hannestad, “What is the lowest possible reheating temperature?,” *Phys.Rev.* **D70** (2004) 043506, [arXiv:astro-ph/0403291 \[astro-ph\]](#).
- [45] J. Brandbyge, S. Hannestad, T. Haugbølle, and Y. Y. Y. Wong, “Neutrinos in Non-linear Structure Formation - The Effect on Halo Properties,” *JCAP* **1009** (2010) 014, [arXiv:1004.4105 \[astro-ph.CO\]](#).
- [46] F. Marulli, C. Carbone, M. Viel, L. Moscardini, and A. Cimatti, “Effects of Massive Neutrinos on the Large-Scale Structure of the Universe,” *Mon.Not.Roy.Astron.Soc.* **418** (2011) 346, [arXiv:1103.0278 \[astro-ph.CO\]](#).
- [47] A. Albrecht, G. Bernstein, R. Cahn, W. L. Freedman, J. Hewitt, *et al.*, “Report of the Dark Energy Task Force,” [arXiv:astro-ph/0609591 \[astro-ph\]](#).
- [48] S. Khedekar and S. Majumdar, “Cosmology with the largest galaxy cluster surveys: Going beyond Fisher matrix forecasts,” *JCAP* **1302** (2013) 030, [arXiv:1210.5586 \[astro-ph.CO\]](#).
- [49] W. Hu, “Crossing the phantom divide: Dark energy internal degrees of freedom,” *Phys.Rev.* **D71** (2005) 047301, [arXiv:astro-ph/0410680 \[astro-ph\]](#).
- [50] M. C. A. Cerbolini, B. Sartoris, J.-Q. Xia, A. Biviano, S. Borgani, *et al.*, “Constraining neutrino properties with a Euclid-like galaxy cluster survey,” [arXiv:1303.4550 \[astro-ph.CO\]](#).